Journal of Materials Chemistry C

ARTICLE

Mapping the Ge/InAl(Ga)As Interfacial Electronic Structure and Strain Relief Mechanism in Germanium Quantum Dots

Received 17th April 2024,
Accepted xxth xx 2024

DOI: 10.1039/x0xx00000x

www.rsc.org/

Mantu K. Hudait*[a], S. Bhattacharya[a], S. Karthikeyan[a], J. Zhao[b], R. J. Bodnar[b], B. A. Magill[c], and G. A. Khodaparast[c]

Abstract

Tensile strained germanium (ε-Ge) has found significant interest due to its unique properties for emerging optoelectronic devices. High tensile strained Ge materials with superior quality are still being investigated due to the intrinsic instability of ε-Ge against the formation of stacking faults (SFs). This work seeks to improve understanding of these limits by closely examining, experimentally, the mechanisms by which tensile strain is relaxed in Ge. Here, ε-Ge layers were grown on highly mismatched $In_{0.53}Ga_{0.47}As$ and $In_{0.51}Al_{0.49}As$ virtual substrates (f = 3.4%), formed as quantum dots (QDs) by molecular beam epitaxy, and their strain relaxation mechanism was analyzed. Both $In_{0.51}Al_{0.49}As$ and $In_{0.53}Ga_{0.47}As$ growth templates were created using an $Al_{0.49}In_{0.51x}(Ga_{0.51})_{1-x}As$ linearly graded metamorphic buffer on GaAs(001)/2° and InP(001)/0.5° substrate, respectively. Fully 3D growth (Volmer-Weber growth mode) due to high tensile strain resulted in Ge QDs with an average diameter and height of ~50 nm and ~20 nm, respectively, and a uniform density of ~320 μm^{-2}. Analysis of interfacial electronic structure using high-resolution transmission electron microscopy collected from the Ge QDs indicated minimal tensile strain was retained in Ge due to SFs formation, corroborated via Raman results. All Ge QDs contain multiple SFs of the close-packed {111} planes nucleated by Shockley partial dislocations with Burger vectors $\boldsymbol{b} = \frac{1}{6}\langle 112\rangle$. The presence of additional misfit dislocations at the $Ge/In_{0.51}Al_{0.49}As$ or $Ge/In_{0.53}Ga_{0.47}As$ heterointerface, not associated with SFs, indicates further relaxation by perfect dislocations with burgers vectors $\boldsymbol{b} = \frac{1}{2}\langle 110\rangle$. The tensile misfit of 3.4% in Ge revealed instability against SFs formation, and the availability of a defect type must have the effect of lowering the critical layer thickness for ε-Ge layers. Thus, the above results suggest the maximum tensile strain amount > 3.4% is not achievable in Ge without the formation of Shockley partial dislocations.

Introduction

Tensile strained germanium (ε-Ge) is being actively investigated for incorporation into next-generation electronic and optoelectronic devices such as tunnel field-effect transistors (TFETs),[1-7] lasers,[8-10] CMOS devices, [11, 12] and LEDs.[13, 14] The surge of interest is primarily driven by its (i) improved compatibility with silicon-based electronics and process flows compared to III-V compound semiconductors, the ability to (ii) enhance hole and electron mobilities, [15, 16] (iii) induce an indirect-to-direct bandgap transition, [10, 17-20] and (iv) assist in tailoring the effective tunnel barrier height in a TFET device. One emerging approach for producing

[a] Advanced Devices & Sustainable Energy Laboratory (ADSEL), Bradley Department of Electrical and Computer Engineering, Virginia Tech, Blacksburg, Virginia 24061, USA. E-mail: mantu@vt.edu
[b] Fluids Research Laboratory, Department of Geosciences, Virginia Tech, Blacksburg, Virginia 24061, USA.
[c] Department of Physics, Virginia Tech, Blacksburg, Virginia, 24061, USA.

tunable tensile strained Ge layers is epitaxial growth on "virtual substrates (VS)" with larger lattice constants. These virtual substrates are created starting from a GaAs, Ge, or Si substrate, and then metamorphically grading the lattice constant, linearly or in steps in the buffer layer, until the desired lattice constant is reached to provide a tensile strain to the Ge layer. The most common method to achieve this is by the growth of an $In_xGa_{1-x}As$ or $In_xAl_{1-x}As$ graded buffer on GaAs(001)[21-23] with surface terminated indium (In) composition in $In_xGa_{1-x}As$ or $In_xAl_{1-x}As$ that will provide variable tensile strain to Ge layer. The advantages of this approach are (i) a high degree of control over the amount of strain (by modulating the In composition, x), and (ii) the ability to incorporate a wide range of strain. However, when the ε-Ge layer thickness is larger than the critical layer thickness for a given misfit, the film will begin to relax by introducing defects and dislocations. The critical layer thickness is influenced by the dislocation type that is energetically favored in the relaxation process. In a diamond and zincblende structure, this dislocation type is usually assumed to be 60° dislocation with Burgers vectors $\boldsymbol{b} = \frac{1}{2} < 110 >$.[24] This assumption is well-supported for the compressive-strain case by ample experimental results in the literature. However, since there are comparatively far fewer experimental studies of tensile-strained relaxation mechanisms, it is unclear how appropriate this assumption is for the tensile-strain system. Such studies are important to better understand the limits of tensile strain that can be incorporated in Ge for photonics. In addition, the higher tensile strain in Ge provided by the underneath large lattice constant virtual substrate can lead to the formation of Ge quantum dots (QDs). Due to the large lattice misfit between the Ge and the underlying layer, the Ge 2D growth mode (Frank-van der Merwe) can be transitioned to an island (3D) growth mode (Volmer-Weber). However, once the size of the QDs is large, the highly tensile strained Ge(001) QDs will relax the lattice misfit by forming defects such as dislocations, stacking faults (SFs), twins, *etc*. Indeed, one can find the relaxation of the 90 nm Ge QD by the creation of SFs, as shown by the cross-sectional transmission electron microscopy (TEM) study reported in Ref. 25. Past research works have also observed a higher tendency for SF formation in tensile strained (001) epitaxial layers due to nucleation of Shockley partial dislocations (SPDs),[22, 24] however, none have studied this phenomenon in highly tensile strained Ge(001) layers. Once we understand the strain relaxation mechanism in Ge QDs, it will open a multitude of device opportunities such as light-emitters for Si-compatible photonics,[11, 26] qubits,[27, 28] photodetectors,[29] and single-hole transistors for charge sensing.[30, 31]

In this investigation, tensile strained Ge layers were grown on a highly tensile-mismatched (a) $In_{0.53}Ga_{0.47}As$ (Sample S1 with targeted growth of 7 nm planar thickness of Ge), (b) $In_{0.53}Ga_{0.47}As$ (Sample S2 with targeted growth of 15 nm planar thickness of Ge), and (c) $In_{0.51}Al_{0.49}As$ (Sample S3 with targeted growth of 10 nm planar thickness of Ge) virtual substrates. The theoretical lattice misfit of ~3.4% was almost the same for all three cases, only the thickness and buffer types (InGaAs versus InAlAs) were carefully selected to understand the relaxation mechanism in the ε-Ge layer. Here, the $Ge/In_{0.51}Al_{0.49}As$ approach for achieving ε-Ge represents a slight variation of the common $Ge/In_{0.53}Ga_{0.47}As$ approach. This approach offers the advantage of a higher valence band offset at the $Ge/In_xAl_{1-x}As$ interface and suppression of parallel conduction due to the higher bandgap buffer layers – two improvements critical for alternate channel Ge-based CMOS applications. A similar structure was recently proposed and experimentally demonstrated for an unstrained (x = 0) Ge layer[11] and metal-oxide-semiconductor (MOS) devices on ε-Ge.[26] Different analytical tools such as surface morphology by atomic force microscopy (AFM), the strain-state by Raman spectroscopy, the relaxation state by x-ray analysis, interfacial electronic structure, and misfit relaxation by high-resolution (HR-TEM) were used for systematic studies of each layer. By examining these QDs using the above analytical tools, we display the intrinsic instability of tensile strained epitaxial Ge(001) against the formation of SFs. Therefore, this research work elucidated the interfacial electronic structure of tensile strained Ge with InGaAs or InAlAs, and their strain relaxation mechanism that limits the tensile strained amount to ε-Ge for electronic and photonic devices.

Experimental

A Materials synthesis

A schematic representation of each layer structure studied in this work is shown in **Fig. 1**. These layer structures were grown using vacuum vacuum-interconnected dual chamber solid source molecular beam epitaxy (MBE) growth system, one for III-V compounds and another for group-IV semiconductors. Semi-insulating GaAs(001) substrates that were 2° off towards <110> direction, and semi-insulating InP(001) substrates that were 0.5° off towards <110> directions, were used for producing these layer structures. GaAs (InP) wafer was heated to ~ 750°C (550°C) substrate temperature (thermocouple temperature) under an arsenic overpressure of $\sim 10^{-5}$ torr for surface oxide desorption inside the III-V MBE chamber. A valved

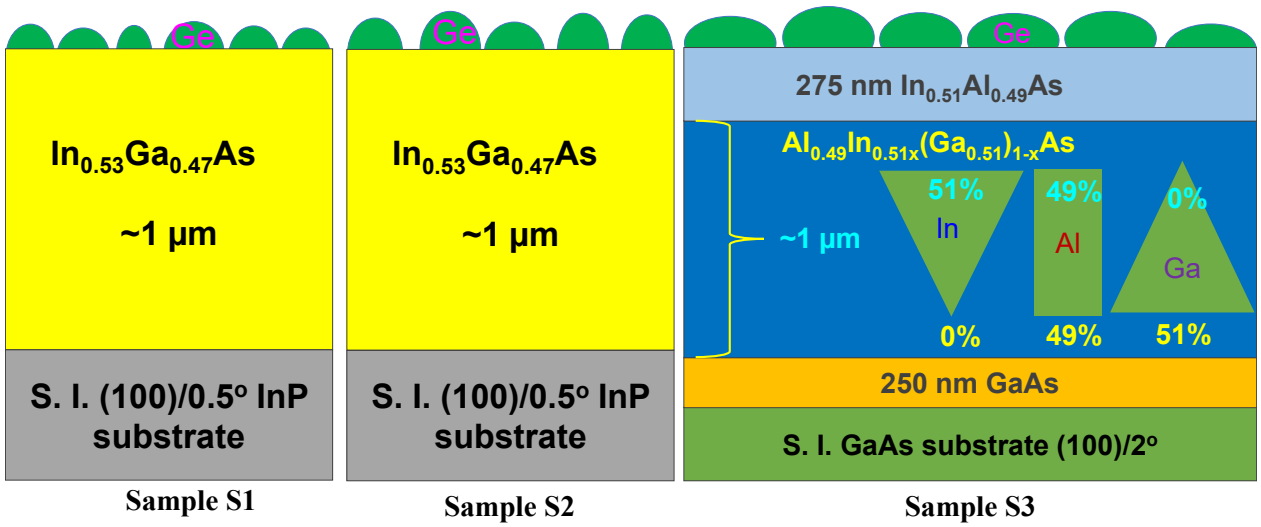

Fig. 1. A schematic representation of the layer structure was used for this work. Here, 7 nm and 15 nm Ge layers were grown on $In_{0.53}Ga_{0.47}As$ virtual substrates (VS), for Sample S1 and S2, respectively. In Sample S3, the aluminum composition was kept constant throughout the quaternary buffer and Ga composition was replaced by In. In this structure, 10 nm Ge layer was deposited on $In_{0.51}Al_{0.49}As$ VS.

cracker arsenic source was used for all the layer structures, where the cracker and bulk temperature were set at 900°C and 340°C, respectively, for arsenic flux (As_2) of ~2×10^{-5} torr. SUMO Ga cell (400 gm capacity), 125 cc In cell, and 60 cc aluminum (Al) cell were used for these structures. The growth rate of Ga, In, and Al was ~ 0.45 µm/hr, 0.5µm/hr, and 0.25 µm/hr, respectively. Each growth rate was measured by reflection high energy electron diffraction (RHEED) intensity oscillation. In addition, each surface reconstruction was monitored during desorption and layer growth. After about 5 min of GaAs layer growth, a (2×4) surface reconstruction was obtained by in-situ RHEED, indicating a clean GaAs surface. A similar observation was made for the InP substrate. First, a 250 nm thick GaAs layer was grown at 650°C to improve the starting surface for the metamorphic buffer in Sample S3. Next, an $Al_{0.49}In_{0.51x}(Ga_{0.51})_{1-x}As$ linear-graded metamorphic buffer was grown at a constant temperature of 420°C, where x was gradually increased from 0 to 1 throughout 1.0 µm of growth. Following completion of the buffer growth, the surface was annealed in-situ for 15 min at 520°C. A 275 nm thick layer of constant composition $In_{0.51}Al_{0.49}As$ was then grown at 530°C. This variety of quaternary buffers has previously been utilized to develop high electron mobility transistor structures on GaAs substrates[32] and may also prove useful for ε-Ge applications.

Due to different surface adatom mobilities of In and Al at any given growth temperature, $In_xAl_{1-x}As$ buffers are challenging to realize in smooth surface morphology and low dislocation densities. To move Al freely on the surface, a higher growth temperature is needed, and this high temperature would lead to the desorption of In from the surface, resulting in higher surface roughness. The quaternary buffer approach allows for a reduction of the growth temperature (replacing some percentage of Al by Ga) while still retaining some of the advantages of having a higher bandgap buffer to suppress parallel conduction. The substrate was then cooled down to < 200°C and removed from the growth chamber to characterize the buffer. The substrate was then cleaved, and a portion was transferred into a second MBE growth chamber dedicated to Ge growth. This sample was outgassed at 300°C for 90 minutes under ultra-high vacuum (~10^{-9} torr). High-temperature oxide desorption was avoided to protect the In composition at the surface and avoid surface roughening. A high-temperature oxide desorption can result in a non-uniform redistribution of surface species due to the large difference in surface mobilities of In and Al. After out-gassing of the sample, a 10 nm (targeted) layer of Ge was grown at 400°C using a low growth rate of ~0.08 Å/s. The Ge growth on the $In_{0.53}Ga_{0.47}As$/InP took place immediately after the $In_{0.53}Ga_{0.47}As$ growth. The $In_{0.53}Ga_{0.47}As$ were grown in a dedicated III-V chamber and transferred under ultra-high vacuum to a separate dedicated Ge growth chamber.

B Materials analysis

The surface morphology of each layer structure was investigated by a Bruker Dimension Icon atomic force microscope in ScanAsyst mode. A scanning electron microscope with an accelerating voltage of ~5 kV was used to determine the surface morphology.

High-resolution X-ray diffraction (HR-XRD) analysis was performed from each structure using a PANalytical X-Pert Pro system equipped with a Cu Kα-1 X-ray source. Symmetric (004) and asymmetric (115) reciprocal space map (RSM) measurements were performed to observe the structural integrity, layer composition, and relaxation. Since the Ge layer forms as QD on underlying VS due to a large lattice misfit, it is challenging to determine the strain state of an individual Ge QD. Raman spectra were recorded using a JY Horiba LabRam HR800 system in the (001) backscattering geometry to identify the vibrational properties of the Ge QDs. An excitation wavelength of 514.53 nm using an Ar^+ laser source by Laser Physics and the gratings of 1800 lines/mm were used during measurement. Laser power at the sample surface during measurement was ~10 mW. Raman measurements were performed on Sample 1 and Sample 2 at three different geometries (ON, above, and below) by focusing the detector so that we could collect Raman signals mostly from Ge QDs or the underlying InGaAs layer.

Thin foil specimens of the sample were prepared for cross-sectional TEM. The foils were made using mechanical polishing, followed by dimpling, and low temperature (~160 K) Ar^+ ion milling to electron transparency. Low-temperature milling was employed to (i) improve the vacuum within the milling chamber by more efficient cold trapping, and (ii) prevent thermal cycling of the foil due to the high energy (2-3 keV) ion beam. Cold trapping is especially important for reducing the amount of sputtered material that is redeposited back onto the foil. The foils were plasma cleaned for 2 minutes with a process gas mixture of 25% oxygen in argon and then transferred directly into a JEOL 2100 TEM with a 200 keV accelerating voltage. Moreover, the optical properties of Ge QDs (Samples S1 and S2) were evaluated at room temperature using photoluminescence (PL) spectroscopy. A Ti: Sapphire laser (720 nm wavelength of excitation) with a repetition rate of 80 MHz, a pulse duration of ~140 fs, and a spot size of ~250 μm in diameter, was used for this measurement. The laser power of 76 W/cm^2 for S1 and 153 W/cm^2 for S2 were used during measurement. The detailed PL measurement setup can be found in Ref. 33. Curve fitting was performed by Origin 2022b using a Gaussian peak fit.

Results and Discussion

A Surface morphology *via* AFM and SEM

Fig. 2(a.i), **(b.i)**, and **(c.i)** shows AFM micrographs of 10 × 10 μm^2 area for Samples S1, S2, and S3, respectively. Samples S1 and S2 do not exhibit a surface cross-hatch pattern, which is expected since the InGaAs layer in each case was grown lattice-matched on the InP substrate. On the other hand, the observed 2D crosshatch pattern from Sample S3 represents the surface morphological signature of a relaxed buffer underneath the Ge QDs. AFM scan is performed over a smaller area (2 × 2 μm^2 and 0.15× 0.15 μm^2) to look for additional surface features and Ge QDs. The result, shown in **Fig. 2(a.ii-iii; b.ii-iii; c.ii-iii)** resolves Ge islands on each surface. The RMS roughness measured from each scan is shown in each figure. The larger area scan does not resolve the QDs since the lateral and horizontal step size between each measurement point is on the order of the spacing between the islands. The Ge islands are observed to uniformly follow the surface of the crosshatch pattern. To determine the height of the dots, a line scan shown in **Fig. 2(a-c: iii)** is taken from the region indicated by the white dotted line in **Fig. 2(a-c: iii)**. The line scan reveals a range of dot heights ~15-25 nm.

To further investigate the surface morphology and to confirm the AFM analysis results above, Sample S3 was

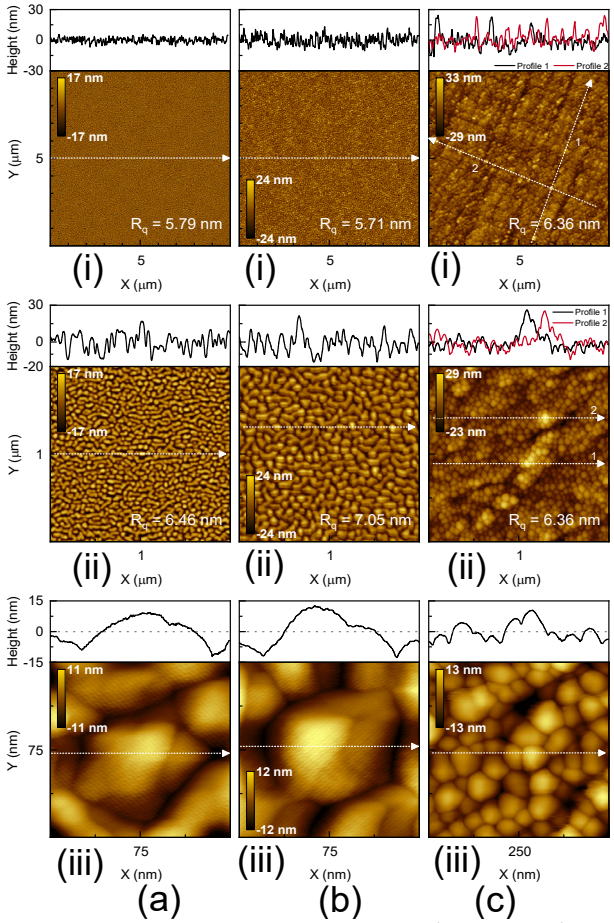

Fig. 2. AFM micrographs of 10 × 10 μm^2, 2 × 2 μm^2, and 0.15× 0.15 μm^2 (0.5× 0.5 μm^2) areas of sample (a) Sample S1, (b) Sample S2, and (c) Sample S3, respectively. A line scan over the Ge QDs corresponding to the dotted white line reveals a range of heights from ~15-25 nm.

studied by SEM secondary electron imaging since the AFM micrograph does not provide whether the QDs coalescence to each other and form a 2D along with 3D growth of Ge. **Fig. 3** shows the sample surface looking directly down along the surface normal. The Ge dots are observed to be uncoalesced and possess a range of diameters of ~20-80 nm with an average of ~50 nm. The density of the dots is ~320 μm^{-2}. The observed long-range uniformity of the Ge QD distribution suggests they do not exhibit any preference in nucleation sites. This result is consistent with the AFM result in **Fig. 2(c.ii)** where the dots are seen to uniformly follow the curvature of the crosshatch ridges. However, from **Fig. 3** it is not clear if a 2D Ge wetting layer (Frank-van der Merwe) formed before the Ge growth transitioned to an island growth mode (Stanski-Krastanov). The strong contrast between the dots and flat regions suggests the two regions may be comprised of different materials, suggesting the absence of a 2D Ge wetting layer. However, this is not conclusive since in secondary electron imaging the topographical contrast mechanism dominates over the Z-contrast mechanism (where Z refers to atomic number). While AFM and SEM analyses are unable to clarify the presence of a wetting layer, cross-sectional TEM images discussed below will reveal that no wetting layer is present and that the growth is indeed fully 3D.

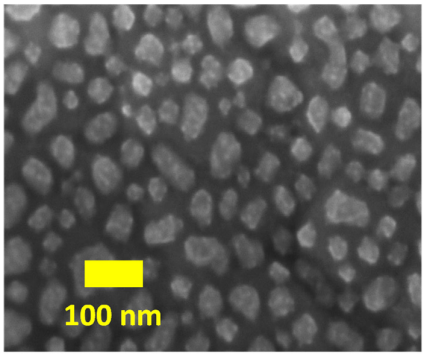

Fig. 3. Top-down SEM secondary electron micrograph showing the surface morphology of Sample S3.

The formation of the islands is driven by the misfit-induced strain at the $Ge/In_{0.51}Al_{0.49}As$ or $Ge/In_{0.53}Ga_{0.47}As$ heterointerface. Tersoff and LeGoues showed that the energy barrier to the formation of island (or surface roughening) scales with ϵ^{-4}, where ϵ is the in-plane misfit strain.[34] While island formation does increase the surface area, it allows for a net decrease of the total energy by permitting partial relaxation of the misfit-induced strain by purely elastic deformation on the growth surface. This relaxation mechanism was shown to compete with relaxation by dislocation formation, which was shown to have a much weaker dependence on ϵ.[35] The difference in the dependencies on misfit for the two mechanisms has dramatic implications for surface morphology and relaxation mechanics. In high misfit systems $\epsilon > \epsilon_0$, the energy barrier for roughening is lower than that for dislocation introduction, and thus the roughening mechanism dominates. For low misfit systems $\epsilon < \epsilon_0$ it is the reverse: (i) it is energetically preferable to relax by dislocation introduction, (ii) the initial dislocations diminish the driving force for roughening, (iii) and the resulting growth is the 2D. This explains why for high misfit systems, QDs can form before any dislocations are introduced, resulting in pseudomorphic strained dots. The crossover points between the two regimes (*i.e.*, the critical misfit ϵ_0) can be determined experimentally for a given set of growth parameters (temperature, growth rate, surfactant, grading rate) and material system. Current research work shows that for the $Ge/In_xAl_{1-x}As$ system, the critical misfit is exceeded since the In composition is 51%. This is the first study, to the author's knowledge, which presents experimental evidence of ϵ_0 for this material system. Since the roughening argument presented by Tersoff and LeGoues [34] did not assume a sign for the misfit, that is whether the misfit is tensile or compressive, the nature of the competition between the relaxation by roughening and relaxation by dislocation formation is not expected to change substantially.

B Vibrational properties *via* Raman

Raman spectroscopy analysis in backscattered geometry was used to determine the strain state in the Ge QDs of Samples S1 and S2 since this technique is widely used by semiconductor industries. Here, the Raman spectra from a Ge QD are similar to the thin film semiconductor heterostructure. To record the information only from the Ge QD, one needs to focus the laser beam so that the intensity of Raman spectra is highest only from the Ge QD. This allows us to determine the longitudinal optical (LO) phonon peak from the Ge QDs. At its minimum spot size, the laser beam (while using the 100 × objective lens) is calibrated to have ~10 μm spot size. However, with the thin Ge QD (Sample S1) on InGaAs, this spot size is way bigger than the size of a single Ge QD. The penetration depth of the 514.53 nm laser in Ge is approximately 19.2 nm. In such a scenario, the incident laser beam does penetrate the InGaAs layer, as the Ge QDs have not coalesced together, as shown in **Fig. 3**. Here, Raman spectra were collected from Samples S1 and S2, shown in **Fig. 4**, where the Raman spectra were obtained from each layer structure in three different measurement conditions, where the laser was focused: above the Ge QDs, ON the QDs and below the QDs. One can find that the Raman signal intensity from the InGaAs layer is dominant in "ON" and "below" cases due to the

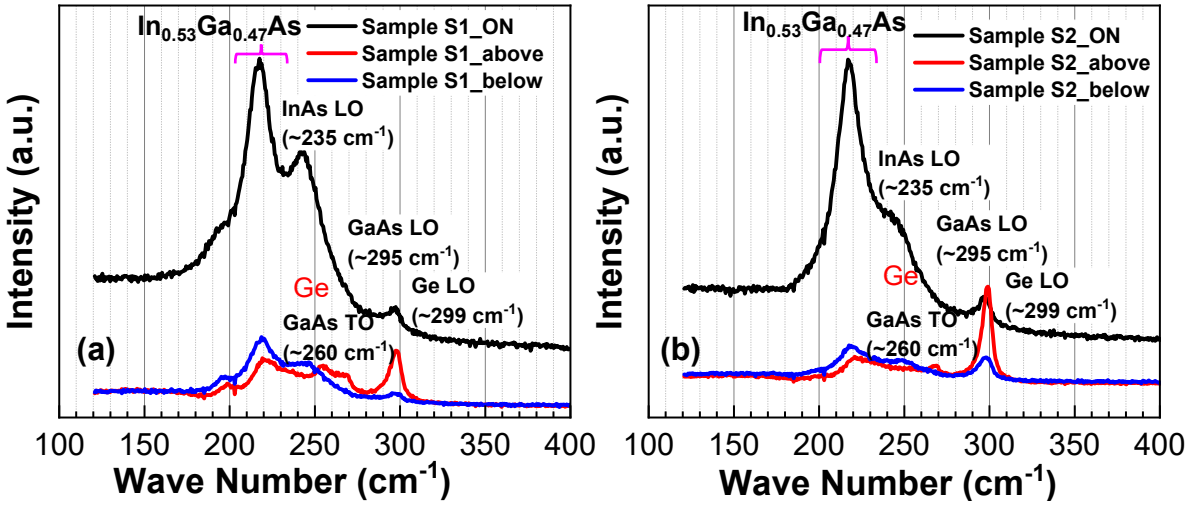

Fig. 4. Raman signal from (a) Sample S1 and (b) Sample S2.

lesser volume of Ge QDs involved in the Raman signal. This is clear from the GaAs (LO, TO) and InAs (LO) phononic peaks in the mixed signal, whereas the peak from the Ge QD gives the true strain calculation. During these measurements, Raman spectra were also recorded from the bulk (100)Ge substrate, and the LO phonon peak was measured at $\omega_o \sim 300.5$ cm^{-1}. Any LO phonon peak shift with respect to ω_o is considered a strain-induced peak shift. The tensile strain represents the shift in peak towards the left and compressive strain towards the right. Each measurement was performed from the three locations of each layer structure. After analyzing the peak separation of each sample, we found that Samples S1 and S2 exhibit 0.38% to 0.65% and 0.25% to 0.38% tensile strain, respectively, indicating that Ge QDs are typically relaxed with no retention of the calculated lattice misfit ~ 3.4% between the Ge and the underlying buffer layer. Note that a large number of Ge QDs were providing the Raman signal since the area of the laser spot size was ~78 μm^2 (ON case). The relaxation properties of Ge QDs can be corroborated by x-ray and further by cross-sectional TEM analysis, discussed below.

C Structural and compositional analysis *via* x-ray

The structural quality and the relaxation state of the Ge QD structures were evaluated using high-resolution x-ray diffraction measurements. **Fig. 5** shows the x-ray rocking curves obtained from the (004) Bragg lines of Ge QDs grown on InP and GaAs substrates of Samples S1, S2, and S3. The angular separation between the diffraction peaks of InP and InGaAs results from the difference in lattice plane spacing, and the InGaAs layer is closely lattice matched with the InP substrate for Samples S1 and S2. The peak separation between the InP substrate and the InGaAs layer is < 0.1°, and it is considered a closely lattice matched InGaAs/InP system. For Sample S2, the broad reciprocal lattice point (RLP) of the Ge layer was observed at the peak position of ~33° (same as the GaAs substrate RLP) indicating the fully relaxed Ge QDs. Here, many Ge QDs provided the x-ray signal from Sample S2. On the other hand, there is no signal from the Ge QDs of Sample S1, due to the thinner volume of Ge materials for exhibiting signal. Furthermore, for the linearly graded $Al_{0.49}In_{0.51x}(Ga_{0.51})_{1-x}As$ buffer, the x-ray rocking curve confirms the gradual change in lattice constant from the GaAs buffer (Sample 3) to the uppermost composition of $In_{0.51}Al_{0.49}As$. The location of the $In_{0.51}Al_{0.49}As$ RLP near the $In_{0.53}Ga_{0.47}As$ RLP, confirms the fully relaxed metamorphic $In_{0.51}Al_{0.49}As/Al_{0.49}In_{0.51x}(Ga_{0.51})_{1-x}As$ buffer. The relaxed Ge RLP would be located at the same position as the

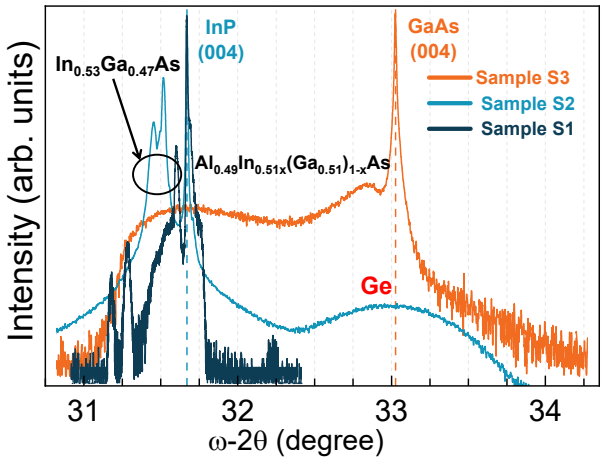

Fig. 5: Symmetric (004) x-ray rocking curves obtained from the 3 Ge QD layer structure studied in this work. Each layer's peak position is identified and listed in this figure.

GaAs substrate RLP. The presence of tensile strain inside the Ge QDs with enough volume[36] could provide a signal other than at the relaxed Ge RLP. Dey *et al*[36] studied the SEM and x-ray images of the QD of the lateral dimensions of 150 nm × 110 nm, which means that the QDs can only provide x-ray signals with larger dimensions. Reciprocal space maps would provide the relaxation state of each Ge QD structure, studied below.

Symmetric (004) and asymmetric (115) RSMs were recorded from layer structures S2 and S3, and only (004) scans from Sample S1. Symmetric (004) RSMs from Samples S1, S2, and S3 are shown in **Fig. 6** (asymmetric scans are not shown here). These RSMs were used to determine the In composition x of the $In_xAl_{1-x}As$ ($In_xGa_{1-x}As$) layer serving as the tensile-mismatched growth template for the Ge. The presence of a small amount of lattice tilt in the InAlAs layer (**Fig. 6c**) complicates the extraction of the in-plane lattice parameter $a_{//}$ from the (115) scan. That the $In_{0.51}Al_{0.49}As$ layer peak does not lie on the same vertical line as the substrate peak in the (004) RSM is direct evidence of lattice tilt. Since the focus of this work is not detailed compositional analysis, no attempt has been made to correct for the tilt, and the assumption of 100% relaxation ($a_{\perp} = a_r$) in the InAlAs layer has been utilized for compositional analysis. This assumption is reasonable since a high degree of relaxation is indicated by the presence of a 2D crosshatch pattern surface morphology seen in **Fig. 2(c.i)**, and it will be further supported by the cross-sectional TEM analysis below. Due to the relatively small volume of Ge in the sample, the scattered x-ray intensity from the QDs coincided with the relaxed Ge RLP (**Fig. 6c**), which indicates that the Ge QDs are relaxed, supported by the Raman measurements where minute amount of tensile strain was determined from Ge QDs. In addition, there is no RSM signal from Sample S1 since it was limited to 7 nm of Ge layer thickness which forms the QDs due to the strain field. The PL measurement will provide whether a thin layer of Ge exists within Sample S1. These results are discussed in the following section.

D Optical properties *via* PL

The optical properties of Sample S1 and S2 were evaluated by photoluminescence spectroscopy at room temperature since this method is widely used to qualify semiconductor materials via different optical transitions. **Fig. 7(a)** and **(b)** show the PL spectra collected from Sample S1 and S2, respectively. Curve fittings to each PL data were carried out to isolate the peak position. Single optical transition, peak position at 0.6716 eV and 0.7598 eV, was observed from Sample S1 and Sample S2, respectively. The emission peak from Sample S1 is

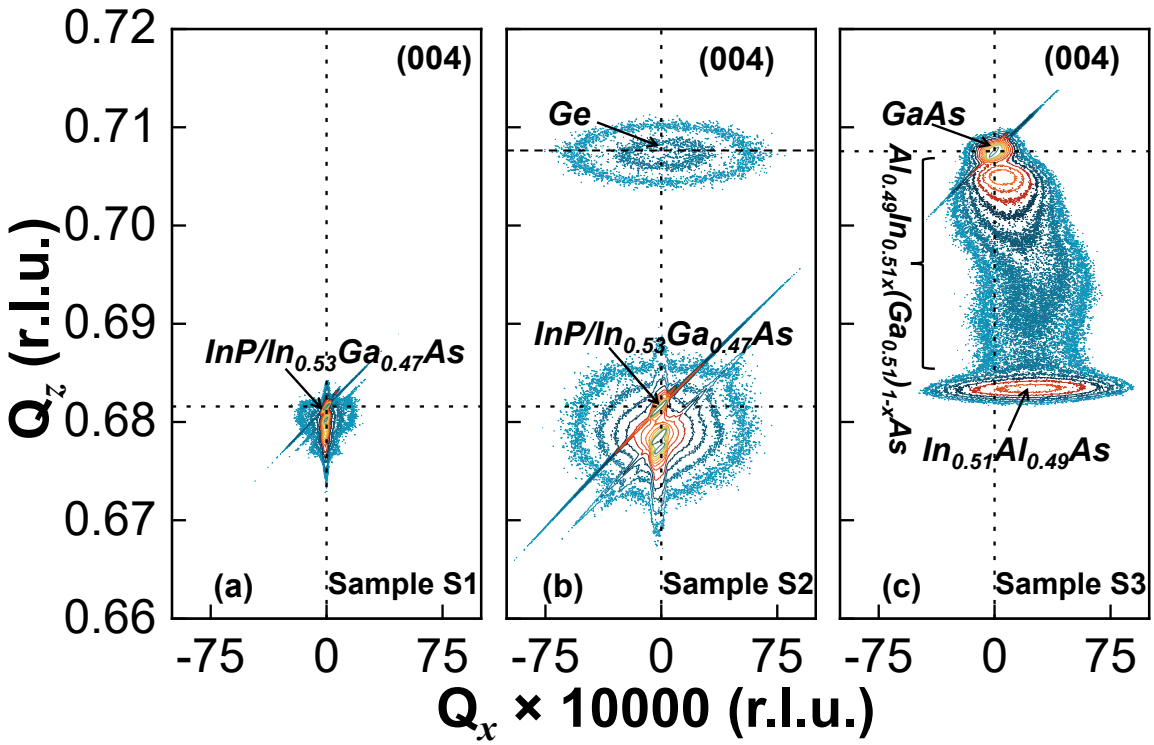

Fig. 6. Symmetric (004) RSMs of Samples S1, S2, and S3. Reciprocal lattice point (RLP) of (a) InP substrate and $In_{0.53}Ga_{0.47}As$ layer. Here the signal from Ge QD is not visible. (b) InP/InGaAs along with relaxed Ge QD RLP, (c) GaAs substrate, graded $Al_{0.49}In_{0.51x}(Ga_{0.51})_{1-x}As$ buffer, and $In_{0.51}Al_{0.49}As$ RLP. The relaxed Ge QD RLP has coincided with GaAs substrate RLP since both materials have almost the same lattice constant.

attributed to carrier recombination from the Ge L-valley to heavy/light hole, *i.e.*, indirect transition. On the other hand, the optical transition from Sample S2 is ascribed as Ge Γ-valley to heavy/light hole recombination, *i.e.*, direct transition. The laser power required to achieve the optical transition from Sample S2 is way higher than from Sample S1 (350 mW versus 150 mW) and no signal was detected at 150 mW from Sample S2. This indicates that the Ge QDs with larger heights relax the strain field and create more SFs than thinner Ge QD samples. The higher laser power generates more carriers, which are now transferred to the Γ-valley. On the other hand, low-power carriers are mostly confined within the L-valley due to the higher density of states. Based on these optical transitions, we infer that the Ge QDs are relaxed. If these QDs are not relaxed, then the peak position would be a longer wavelength due to the reduction of the Ge bandgap.

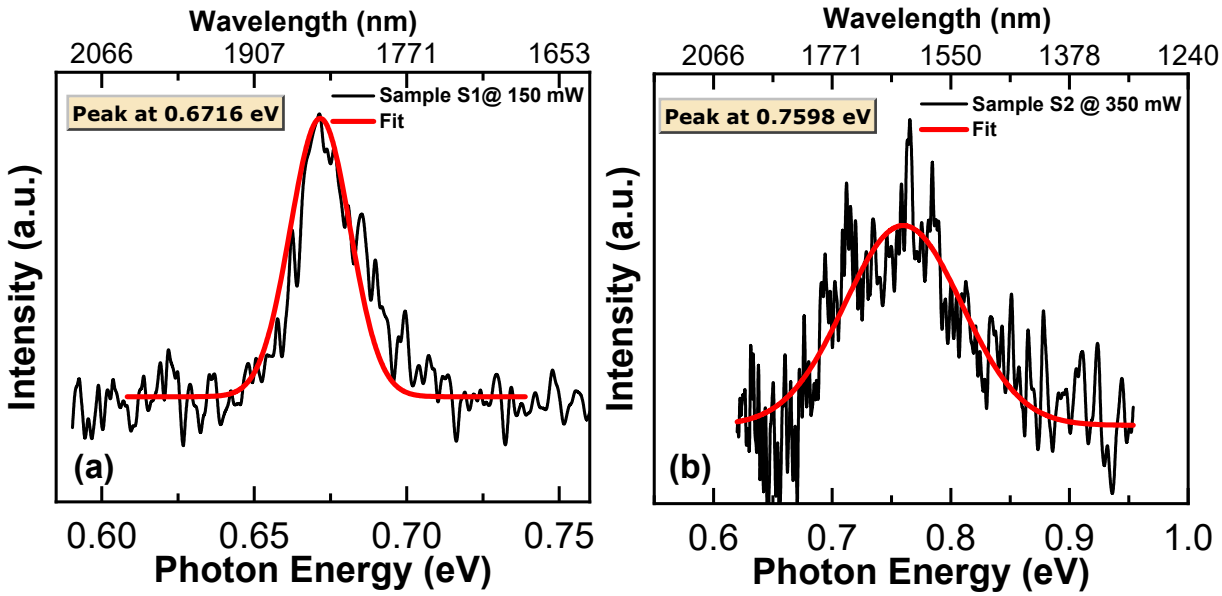

Fig. 7. PL signal from (a) Ge/$In_{0.53}Ga_{0.47}As$/InP (Sample S1) and (b) Ge/$In_{0.53}Ga_{0.47}As$/InP (Sample S2) structures.

E Heterointerface analysis *via* TEM

Fig. 8(a) and **(b)** show a cross-sectional TEM micrograph of the full layer structure for Samples S2 and S3, respectively. One can find that the lattice mismatch-induced defects and dislocations are confined within the graded quaternary $Al_{0.49}In_{0.51x}(Ga_{0.51})_{1-x}As$ buffer on GaAs substrate, and the $In_{0.53}Ga_{0.47}As$ layer is lattice matched to InP substrate. The constant composition $In_{0.51}Al_{0.49}As$ and $In_{0.53}Ga_{0.47}As$ layers served as strain templates to the Ge layer. In both samples, a high degree of strain-induced fully 3D Ge growth was observed.[34] The average island height on the InGaAs and InAlAs virtual substrates is ~ 40 nm and 20 nm, respectively. The difference in island size is due to a slightly longer duration of Ge layer growth for the InGaAs sample, as discussed in the experimental section. The InAlAs sample contained only uncoalesced islands, while the InGaAs sample contained a mixture of coalesced and uncoalesced islands as shown in **Fig. 8(a)**. Since dislocation-free Ge islands with greater heights have been observed for compressive growth on higher mismatch Si substrates,[37] it seems plausible that the Ge islands in both samples in this work might contain considerable tensile strain due to lower lattice misfit. Due to the small volume of Ge in these samples, x-ray diffraction methods to evaluate precise strain could not be applied. By knowing the RLP position of the relaxed Ge, we can infer that the Ge QDs are relaxed in Sample S2. However, Raman measurement shows only a minute amount (0.25% to 0.38%) of tensile strain present within the Ge layer (Sample S2). A cross-sectional HR-TEM micrograph of representative Ge QDs from Sample S2 and S3 are shown in **Figs. 9(a)** and **(b)**, respectively. The specimen foil has been tilted so the incident beam direction is aligned to the $[\bar{1}10]$ crystallographic direction. Stacking faults of particular interest are marked by the yellow dotted lines and these SFs are also associated with twin boundaries, as shown in **Fig. 9(b)**. In addition, two micro-twins have annihilated each other, as shown in the inset of **Fig. 9 (b).** Further investigation of the Ge QDs grown on InGaAs VS, reveals defect-free regions of InGaAs buffer and Ge QDs, as shown in **Fig. 10(a)**. Further, Ge QD showing the defect-free region and clusters of SFs (obtained by inverse-Fourier filtered

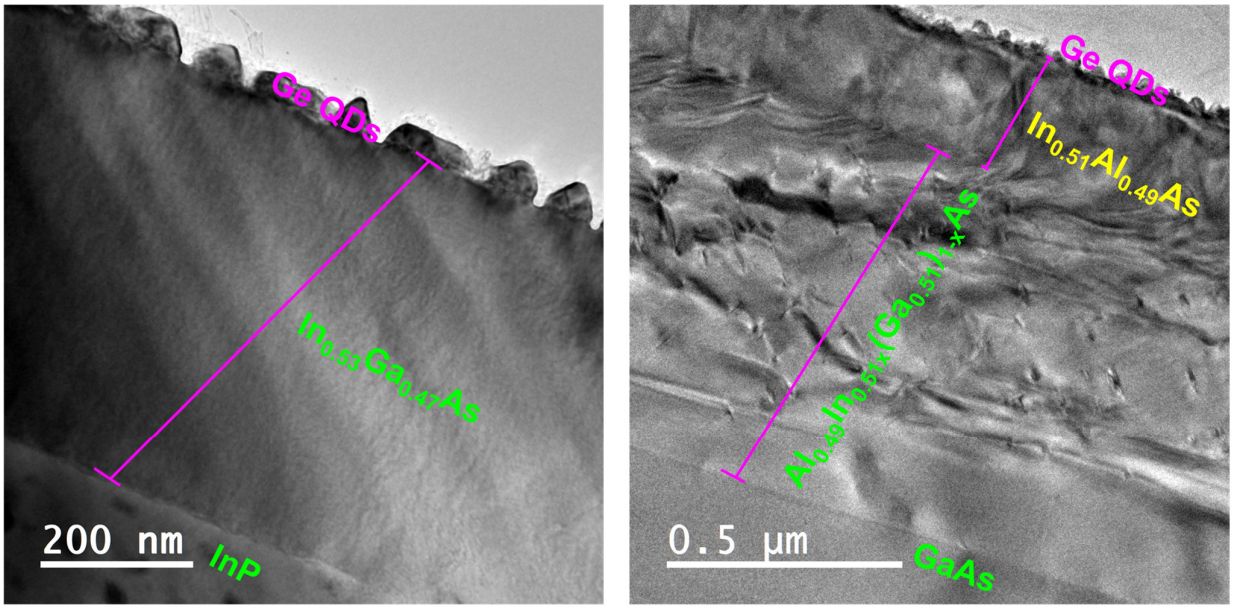

Fig. 8. Bright field cross-sectional TEM micrographs of the (a) $Ge/In_{0.53}Ga_{0.47}As/InP$ (Sample S2) and (b) $Ge/In_{0.51}Al_{0.49}As/Al_{0.49}In_{0.51x}(Ga_{0.51})_{1-x}As/GaAs$ (Sample S3) layers structures examined in this work.

micrographs), relieved the strain from Ge QD. One can find that certain parts of the Ge QD exhibit defect-free regions, but the net QD is relaxed by generating clusters of SFs, similar to those reported in Ref. 25. The same types of defects were observed in Ge QDs from both samples.

As discussed above, the Ge QDs contain a negligible amount of tensile strain, and a high degree of relaxation is supported by the presence of both SFs and classic 60° misfit dislocations at the Ge/VS interfaces, as shown by HR-TEM. Relaxed islands grown on a highly tensile-mismatched (001) VS here contrast sharply with previous results of larger islands grown dislocation-free on a more

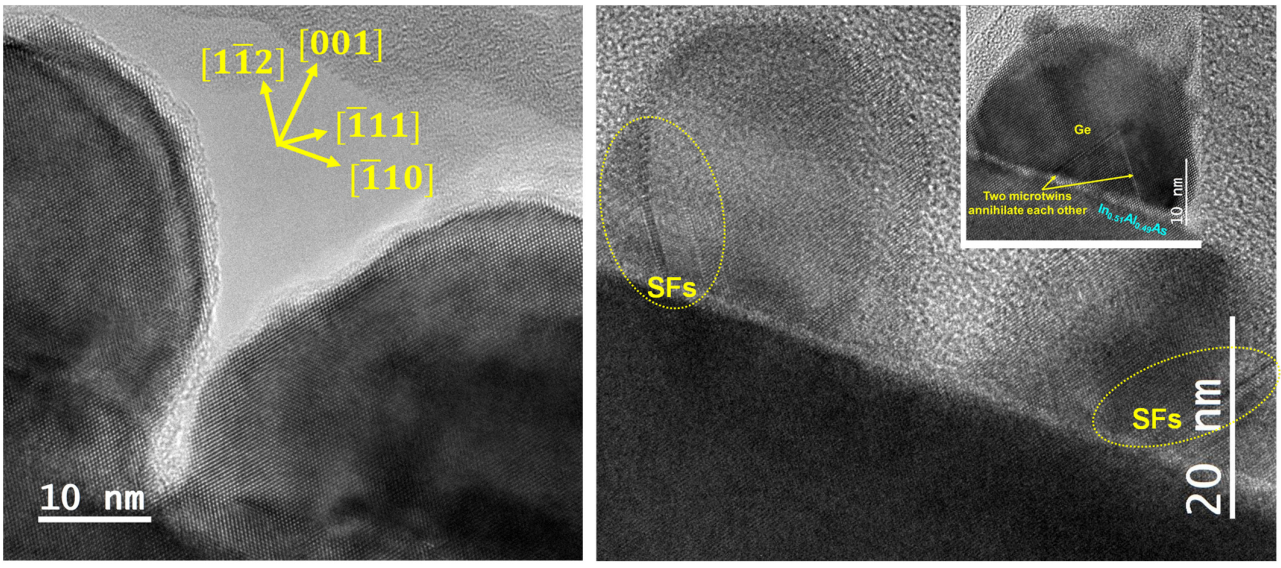

Fig. 9. A cross-sectional TEM micrograph of representative Ge QDs from Samples S2 and S3. (a) Two Ge QDs are separated and (b) SFs (marked by yellow dotted line) are observed in each QD. Inset shows two micro-twins from one Ge QD have annihilated each other.

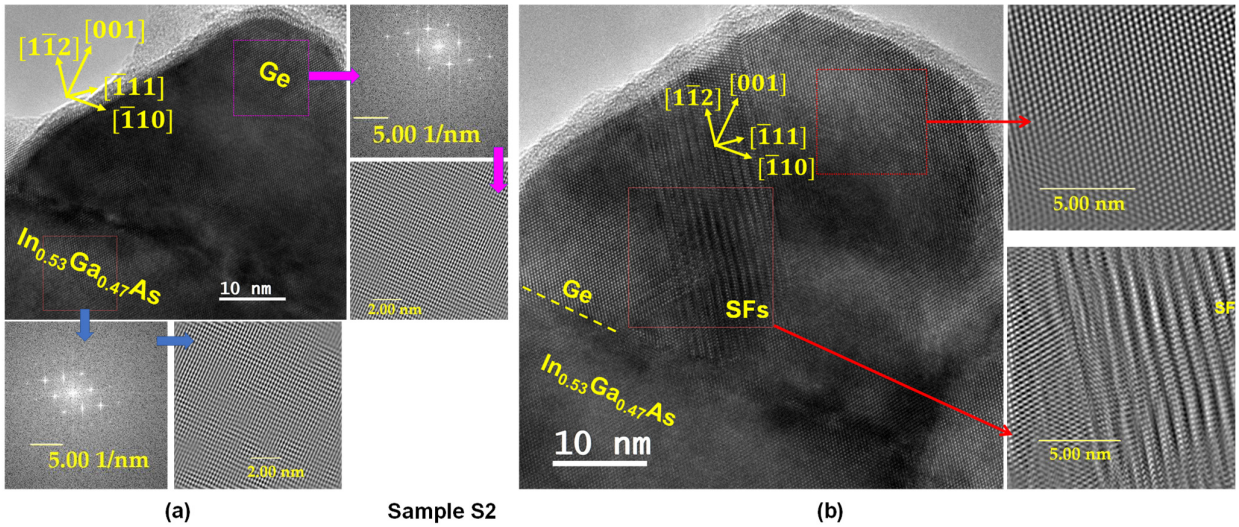

Fig. 10. A cross-sectional TEM micrograph of a representative Ge QD from Sample S2. (a) Ge QD along with two regions marked by two boxes: Fast Fourier transform (FFT) in the Ge QD and underlying $In_{0.53}Ga_{0.47}As$ layer along with inverse FFT of the same. (b) Ge QD showing the defect-free region and clusters of SFs (by inverse-Fourier filtered micrographs), relieved the strain from Ge QD.

highly compressive-mismatched Si(001) substrate.[37] These divergent results demonstrate a central difference between the relaxation mechanics of the compressive-high misfit regime and the tensile-high misfit regime. The relaxation by Shockley partial dislocations (SPDs) in addition to perfect 60° dislocations in the tensile case (i) directly results in much higher SF densities and (ii) can facilitate faster relaxation since the Burgers vector of the SPDs is smaller and is completely aligned with the resolved shear stress on the {111} planes.[38] These effects are further supported by experimental reports based on $GaP/Ga_{0.3}As_{0.7}P/GaP(001)$ double heterostructures,[39] and comparisons of Si_xGe_{1-x} alloys grown on tensile mismatched Ge(001) or compressive mismatched Si(001).[40] It is well established that relaxation by surface roughening competes with relaxation by dislocation introduction in strained-layer epitaxy.[34] One conclusion that this work along with Refs. 37-41 supports that in tensile (001) layer epitaxy, there is an additional competition: the relaxation by perfect 60° dislocations competing with relaxation by SPDs with SFs.

The formation of the SFs themselves is explained by a mechanism proposed by Marée *et al.* and is based on the disassociation of the classic 60° dislocations into a pair of SPDs.[38] **Fig. 11** shows a diagram of the SF formation mechanism using the hard-packed sphere model. The directions shown correspond to the case where the misfit is tensile, and the growth direction is (001). $\mathbf{b_0}$ represents the Burgers vector of the classic 60° dislocations and is a full lattice translation vector (*i.e.* a perfect dislocation). In response to the resolved shear stress $\boldsymbol{\tau}$ due to the mismatch, each sphere in the top plane shears from one *A* site to an adjacent *A* site, restoring the correct *ABCABC* stacking order but leaving a misfit dislocation in the interface. It is believed that in executing the $\mathbf{b_0}$ translation the shearing plane does not move directly over the tops of the *B* spheres (a high energy path), but instead follows the lower energy path between the *B* spheres. This path corresponds to making the translation $\mathbf{b_1}$ and then $\mathbf{b_2}$ successively, where $\mathbf{b_1}$ and $\mathbf{b_2}$ are Burgers vectors for a Shockley partial dislocation pair, and is equivalent to the Burgers vector reaction given by,

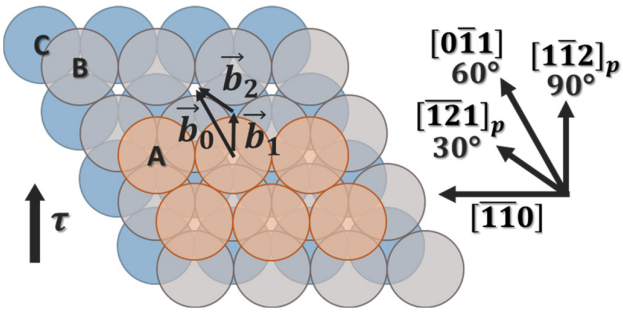

Fig. 11. A hard-packed sphere model of the $(\bar{1}11)$ planes showing how the perfect 60° dislocations with Burgers vector $\boldsymbol{b_0}$ is comprised of two Shockley partial dislocations with Burgers vectors $\boldsymbol{b_1}$ and $\boldsymbol{b_2}$. If the two partials do not nucleate and glide together as a pair, an SF is formed along the planar length of the crystal between them. $\boldsymbol{\tau}$ represents the resolved shear stress due to the tensile misfit strain on the $(\bar{1}11)$ planes. The top-down direction looking into the diagram is $[\bar{1}11]$. The direction of the dislocation line in all cases is $[\bar{1}\bar{1}0]$. The dislocations take their name from the angle their Burgers vector makes with the dislocation line.

$$\boldsymbol{b}_1 + \boldsymbol{b}_2 \rightarrow \boldsymbol{b}_0 \qquad \frac{1}{6}[1\bar{1}2] + \frac{1}{6}[\bar{1}\bar{1}2] \rightarrow \frac{1}{2}[0\bar{1}1]$$

where all three vectors lie in the same {111} slip plane. However, if only translation $\mathbf{b_1}$ can be made and not $\mathbf{b_2}$, the top plane now occupies *C* sites (believed to be local energy minima) and the stacking order is disrupted. The stacking order is now *ABCBCABC* – an *A* plane is missing, and an intrinsic SF has been introduced. This situation is observed in **Fig. 10(b)**. The angle between the resolved shear stress $\boldsymbol{\tau}$ and the vectors $\mathbf{b_1}$ and $\mathbf{b_2}$, and the order in which the partial dislocations $\mathbf{b_1}$ and $\mathbf{b_2}$ must nucleate, play important roles in determining when this situation is likely to occur. In the case where the strain is tensile and the growth direction is (001), as shown in **Fig. 11**, the angle between $\boldsymbol{\tau}$ and $\mathbf{b_1}$ and $\mathbf{b_2}$ is 0° and 60° respectively, corresponding to a factor of two difference in the shear force exerted on the 90° partial compared to that for the 30° partial dislocation. When the strain is compressive, the vectors $\mathbf{b_0}$, $\mathbf{b_1}$, $\mathbf{b_2}$, and $\boldsymbol{\tau}$ are inverted as they are shown in **Fig. 11**.[38] Now the 30° partial, which is poorly aligned with $\boldsymbol{\tau}$, must lead in the reaction sequence, shown above equation. Once the 30° partial nucleates, the 90° partial follows immediately since $\boldsymbol{\tau}$ acts on the 90° more efficiently, resulting in the annihilation of the SFs and the formation of a classic 60° perfect dislocation. It is important to note that since the resolved shear stress acts on the 30° partial inefficiently, and since the 30° partial must nucleate before the 90° partial, the energy barrier for nucleating a dislocation can be higher in the compressive case than in the tensile case. In the tensile case, the 90° partial leads the reaction sequence, leaving open the possibility that the resolved shear stress may be sufficient to nucleate the 90° partial but not the 30° partial, which would result in an SF. This may help explain why Eaglesham and Cerullo observed dislocation-free compressive Ge/Si(001) islands up to 50 nm in height,[37] and why a similar result was not observed in this work for a tensile case. Marée *et al.* used this mechanism to explain a difference in the number of SFs experimentally observed between the tensile Si/GaP(001) interface and the compressive $In_{0.07}Ga_{0.93}As$/GaAs(001) interface,[38] but until now there have been no reports of this occurring in tensile Ge/III-V interfaces. However, Wang *et al.* [25] demonstrated Ge QDs using selective oxidation of poly-$Si_{1-x}Ge_x$ lithographically patterned structures over Si_3N_4 layers, where 60 nm and 90 nm Ge QDs were relaxed. In addition, Chen *et al.*[42] demonstrated the Ge QDs on InAlAs and InGaAs where extensive defects were observed at the Ge/InGaAs heterointerface. This work confirms the instability of tensile Ge/III-V heterointerface against the formation of SFs – a potential concern since SFs can be extremely detrimental to device performance at highly tensile strained systems. However, the exact boundary of lattice misfit is not known where the tensile strain is inhibiting the formation of SFs. This work elucidated that the maximum biaxial tensile strain in Ge cannot be as high as 3.4%, without the formation of SFs.

If the growth direction is (011) or (111) instead of (001), the vectors in **Fig. 11** are again inverted.[43] The result is that now the 30° partial must nucleate first in the tensile case and the 90° must nucleate first in the compressive case, rendering compressive films now unstable to SF formation instead of tensile films. This is supported by experimental studies of SFs in compressive non-(001) films.[44, 45] In these reports, researchers found the critical layer thickness was shifted lower in compressive-(011) films as compared to compressive-(001) films. This is because, in compressive-(011) films, the Burgers vector of the 90° SPD is completely aligned with $\boldsymbol{\tau}$ on the inclined {111} planes (as shown in **Fig. 11**) and is, therefore, more efficient at accommodating that stress. This fact does not change between the tensile-(001) interface and the compressive-(011) interface. Therefore, for at least some misfit regime, the critical layer thickness for the tensile-(001) interface should also be shifted lower (with respect to the compressive-(001) case). It is also worth noting that since this work is based on observations of uncoalesced islands, this mechanism for relaxation by Shockley partial dislocations with SFs is now shown to be independent of any dislocation interaction that takes place during the coalescing of growing islands. This is the first work, to the author's knowledge, that has observed this mechanism in uncoalesced islands.

Conclusion

Highly tensile strained Ge layers were grown on two different metamorphic buffers, $In_{0.53}Ga_{0.47}As$ and $In_{0.51}Al_{0.49}As$ by solid source molecular beam epitaxy, and their relaxation mechanism were investigated. Due to the large lattice misfit, the Ge layer formed as quantum dots with an average diameter and height of ~50 nm and ~20 nm, respectively, and a density of ~320 μm^{-2} uniformly distributed over the underlying buffer. The instability of highly tensile Ge(001) epitaxial layers against stacking fault formation was experimentally demonstrated on III-V buffers. HR-TEM indicated that the Ge QDs retained minimal tensile strain, and most of the lattice misfit strain (f = 3.5%) was relaxed by creating the SFs. The mechanism driving the formation of the SFs is consistent with the model proposed by Marée *et al*. for relaxation of (001) oriented tensile layers by nucleation of Shockley partial dislocations. All Ge QDs contain SFs

of the close-packed {111} planes nucleated by Shockley partial dislocations with burger vectors $\boldsymbol{b} = \frac{1}{6}\langle 112 \rangle$. The SFs arise from a higher net force on the leading 90° disassociated component of the classic 60° dislocations, compared to the trailing 30° disassociated component. This difference in forces can result in the separation or disassociation of Shockley partial dislocation pairs, inhibiting them from traveling together, i.e. 60° dislocations. In the low and intermediate tensile-misfit regime ($\epsilon < 2.0$) undisassociated 60° dislocations remain energetically favorable due to the additional energy required to form a stacking fault. The required stacking fault energy effectively acts as an additional force on each partial dislocation holding the Shockley pair together. As a result, the low and immediate tensile-misfit regimes are much less affected by the instability phenomena, and the tensile strain needed to achieve a Ge direct bandgap is reported to be less than 2.0%,[15, 20] suggesting direct bandgap Ge can be achieved before triggering the SF formation instability. Hence, the maximum tensile strain that can be realized in Ge without the formation of Shockley partial dislocations is lower than 3%. Further investigations are necessary as a function of tensile strain in Ge on III-V virtual substrate or thinner quantum dots that can retain the strain without relaxation by creating stacking faults.

Conflicts of interest

There are no conflicts to declare.

Data availability

This research paper is purely experimental findings, and no external data or software was used to develop any conclusions. However, if any measurement data is required, those can be available upon request from the corresponding author.

Acknowledgments

M. K. H. and S.K. acknowledge partial support from the NSF under grant number ECCS-2042079, a US-Ireland Joint R&D Program and Virginia Tech Nanoscale Characterization and Fabrication Laboratory and Virginia Tech Nanofabrication facilities for assistance during materials analysis. M. K. H. acknowledges the contribution of M. Clavel for assisting epitaxial growth and P. Goley for TEM/SEM measurements and technical discussions. In addition, the authors acknowledge Virginia Tech College of Engineering for seed funding for quantum technology research. G. A. K. acknowledges the support of the Air Force Office of Scientific Research DURIP funding (FA9550-16-1-0358).

Author information

Corresponding Author *Tel: (540) 231-6663. E-mail: mantu@vt.edu.

Author contribution

The manuscript was written through the contributions of all authors. All authors have approved the final version of the manuscript.

Notes and references

1 Y. Zhu, D. Maurya, S. Priya, and M. K. Hudait, *ACS Appl. Electron. Mater.*, 2014, **6**, 4947.

2 K. -H. Kao, A. S. Verhulst, M. Van de Put, W. G. Vandenberghe, B. Soree, W. Magnus, and K. De Meyer, *J. Appl. Phys.*, 2014, **115**, 044505.

3 S. Wirths, A. Tiedemann, Z. Ikonic, P. Harrison, B. Holländer, T. Stoica, G. Mussler, M. Myronov, J. Hartmann and D. Grützmacher, *Appl. Phys. Lett.*, 2013, **102**, 192103.

4 J. -S. Liu, M. Clavel, and M. K. Hudait, *IEEE Trans. Electron Dev.*, 2015, **62**, 3223.

5 M. Clavel, D. Saladukha, P. Goley, T. J. Ochalski, F. Murphy-Armando, R. J. Bodnar, and M. K. Hudait, *IEEE J. Electron Dev. Soc.* (Special Issue: Steep Sub-threshold Transistor), 2015, **3**, 184.

6 J. -S. Liu, M. Clavel, and M. K. Hudait, *IEEE Trans. Electron Dev.*, 2017, **64**, 2193.

7 J. -S. Liu, M. Clavel, and M. K. Hudait, *IEEE J. Electron Dev. Soc*., 2019, **7**, 210.

8 J. Liu, X. Sun, D. Pan, X. Wang, L. C. Kimerling, T. L. Koch, and J. Michel, *Optics Express* 2007, **15**, 11272.

9 R. Soref, *Nat. Photonics* 2010, **4**, 495.

10 M. K. Hudait, F. Murphy-Armando, D. Saladukha, M. B Clavel, P. S Goley, D. Maurya, S. Bhattacharya, T. J. Ochalski, *ACS Appl. Electron. Mater.* 2021, **10**, 4535-4547.

11 M. K. Hudait, M. B. Clavel, S. Karthikeyan, and R. Bodnar, *ACS Appl. Electron. Mater.,* 2023, **5**, 4792.

12 Y. -J. Yang, W. Ho, C.-F. Huang, S. Chang, and C. Liu, *Appl. Phys. Lett.*, 2007, **91**, 102103.

13 X. Sun, J. Liu, L. C. Kimerling, and J. Michel, *Optics letters* 2009, **34**, 1198.

14 J. R. Jain, A. Hryciw, T. M. Baer, D. A. Miller, M. L. Brongersma, and R. T. Howe, *Nat. Photonics* 2012, **6**, 398.

15 M. V. Fischetti and S. E. Laux, *J. Appl. Phys.*, 1996, **80**, 2234.

16 M. B. Clavel, F. Murphy-Armando, Y. Xie, K. T. Henry, M. Kuhn, R. J. Bodnar, G. A. Khodaparast, D. Smirnov, J. J. Heremans, and M. K. Hudait, *Phys. Rev. Appl.*, 2022, **18**, 064083.

17 D. Saladukha, M. B. Clavel, F. Murphy-Armando, G. Greene-Diniz, M. Gruening, M. K. Hudait, and T. J. Ochalski, *Phys. Rev.* B 2018, **97**, 195304.

18 M. K. Hudait, M. Clavel; L. Lester; D. Saladukha; T. Ochalski; F. Murphy-Armando, *Proc. SPIE 9755, Quantum Sensing and Nano Electronics and Photonics XIII, 97550Y* (February 13, **2016**).

19 M. Clavel, D. Saladukha, P. Goley, T. J. Ochalski, F. Murphy-Armando, R. J. Bodnar, and M. K. Hudait, *ACS Appl. Mater. Inter.*, 2015, **7**, 26470.

20 R. A. Soref and L. Friedman, *Superlattices and microstructures* 1993, **14**, 189 (1993).

21 R. Jakomin, M. de Kersauson, M. El Kurdi, L. Largeau, O. Mauguin, G. Beaudoin, S. Sauvage, R. Ossikovski, G. Ndong, M. Chaigneau, I. Sagnes, and P. Boucaud, *Appl. Phys. Lett.*, 2011, **98**, 091901.

22 Y. J. Huo, H. Lin, R. Chen, M. Makarova, Y. W. Rong, M. Y. Li, T. I. Kamins, J. Vuckovic, and J. S. Harris, *Appl. Phys. Lett.*, 2011, **98**, 011111.

23 Y. Bai, K. E. Lee, C. Cheng, M. L. Lee, and E. A. Fitzgerald, *J. Appl. Phys.*, 2008, **104**, 084518.

24 E. Fitzgerald, *Mater. Sci. Reports* 1991, **7**, 87.

25 I-Hsiang Wang, Po-Yu Hong, Kang-Ping Peng, Horng-Chih Lin, Thomas George, and Pei-Wen Li, *2020 IEEE International Electron Devices Meeting* (IEDM), 12-18 December 2020. pp. 841-844.

26 M. K. Hudait, M. Clavel, P. Goley, N. Jain, and Y. Zhu, *Scientific Rep.,* 2014, **4**, 6964.

27 L. A. Terrazos, E. Marcellina, Zhanning Wang, S. N. Coppersmith, Mark Friesen, A. R. Hamilton, Xuedong Hu, Belita Koiller, A. L. Saraiva, Dimitrie Culcer, and Rodrigo B. Capaz, *Phys. Rev.* B 2021, **103**, 12.

28 A. Sammak, D. Sabbagh, N. W. Hendrickx, M. Lodari, B. P. Wuetz, A. Tosato, L. Yeoh, M. Bollani, M. Virgilio, M. A. Schubert, P. Zaumseil, G. Capellini, M. Veldhorst, G. Scappucci, *Adv. Funct. Mater.* 2019, **29**, 1807613.

29 S. Siontas, D. Li, H. Wang, A. A.V.P.S, A. Zaslavsky, D. Pacifici, *Mater. Sci. Semiconductor Proc.* 2019, **92**, 19-27.

30 C. -C. Lai, R. C. Pan, I. -H. Wang, T. George, H. -C. Lin and P. -W. Li, *IEEE J. Electron Dev. Soc.* 2023*,* **11**, 54.

31 P. Y. Hong, C. C. Lai, T. Tsai, H. -C. Lin, T. George, P. -W. Li, and D. M. T. Kuo, *Sci. Rep.,* 2023*,* **13**, 14333.

32 M. Haupt, K. Köhler, P. Ganser, S. Emminger, S. Müller, and W. Rothemund, *Appl. Phys. Lett.*, 1996, **69**, 412.

33 M. K. Hudait, M. Meeker, J.-S. Liu, M. B. Clavel, S. Bhattacharya and G. A. Khodaparast, *Opt. Mater.*, 2022, **131**, 112633.

34 J. Tersoff and F. LeGoues, *Phys. Rev. Lett.,* 1994, **72**, 3570.

35 F. LeGoues, P. Mooney, and J. Tersoff, *Phys. Rev. Lett.,* 1993, **71**, 396.

36 A. B. Dey, M. K. Sanyal, A. Schropp, S. Achilles, T. F. Keller, I. Farrer, D. A. Ritchie, F. Bertram, C. G. Schroer, and O. H. Seeck, *ACS Nano* 2023, **17**, 16080.

37 D. Eaglesham and M. Cerullo, *Phys. Rev. Lett.,* 1990, **64**, 1943.

38 P. Maree, J. Barbour, J. Van der Veen, K. Kavanagh, C. Bulle-Lieuwma, and M. Viegers, *J. Appl. Phys.*, 1987, **62**, 4413.

39 J. Petruzzello and M. Leys, *Appl. Phys. Lett.*, 1988, **53**, 2414.

40 W. Wegscheider and H. Cerva, *J. Vac. Sci. Technol.* B, 1993, **11**, 1056.

41 C. Claeys and E. Simoen, *Extended defects in germanium: fundamental and technological aspects* (Springer, 2008), Vol. 118.

42 Q. Chen, L. Zhang, Y. Song, X. Chen, S. Koelling, Z. Zhang, Y. Li, P. M. Koenraad, J. Shao, C. S. Tan, S. Wang, and Q. Gong, *ACS Appl. Nano Mater.,* 2021, **4**, 897.

43 E. Kvam and R. Hull, *J. Appl. Phys.*, 1993, **73**, 7407.

44 R. Hull, J. Bean, L. Peticolas, and D. Bahnck, *Appl. Phys. Lett.*, 1991, **59**, 964.

45 R. Hull, J. Bean, L. Peticolas, D. Bahnck, B. Weir, and L. Feldman, *Appl. Phys. Lett.*, 1992, **61**, 2802.